

# Multiscale energy budget of inertially driven turbulence in normal and superfluid helium

Fatimata Sy, Pantxo Diribarne , and Bernard Rousset <sup>\*</sup>  
*dSBT/IRIG CEA, Université Grenoble Alpes - F-38054 Grenoble, France*

Mathieu Gibert   
*Institut NEEL, CNRS, Université Grenoble Alpes - F-38042 Grenoble, France*

Mickael Bourgoïn  
*Laboratoire de Physique, Univ. Lyon, ENS de Lyon, Univ. Claude Bernard Lyon 1,  
CNRS, 69007 Lyon, France*



(Received 25 November 2020; accepted 3 May 2021; published 8 June 2021)

In this paper we present a novel hydrodynamic experiment using liquid  $^4\text{He}$ . Lagrangian trajectories are obtained using two-dimensional particle tracking on hollow glass microspheres in a cryogenic liquid helium turbulent flow. The flow is forced inertially by a canonical oscillating grid, both below and above the superfluid transition. This allows for a direct comparison of the Lagrangian statistics in the normal (He I) and superfluid (He II) phases. The high temporal resolution allows us to resolve the velocity fluctuations at integral and inertial scales and, most importantly, assess the noise contribution. The careful analysis of velocity fluctuations, acceleration fluctuations, and pair dispersion, allows us to extract estimates of the energy-injection rate at large scale, the energy flux cascading through inertial scales, and the dissipation rate at small scale, and therefore build the energy budget in both the normal and superfluid phases. We find that, within experimental uncertainty, the statistical features of turbulence and the energy budget in superfluid helium is indistinguishable from those of normal helium, highlighting the importance of conducting experiments in both He I and He II to draw meaningful conclusions, because deviations from the theoretical predictions may arise from noise contributions or deviation from the homogeneous and isotropic approximations.

DOI: [10.1103/PhysRevFluids.6.064604](https://doi.org/10.1103/PhysRevFluids.6.064604)

## I. INTRODUCTION

Liquid helium experiments offer a unique way to investigate developed turbulence in laboratory-scale facilities. Liquid helium, in its normal state (He I), has indeed a very low kinematic viscosity  $\nu$ . In addition, one of the most striking features of liquid helium is the superfluid state (He II), where the kinematic viscosity eventually vanishes below a critical temperature  $T_\lambda \approx 2.17$  K.

While He I follows a classical Navier-Stokes equation dynamics for a viscous newtonian fluid, He II is usually described as a mixture of a normal (viscous) and a superfluid (inviscid) components with a relative fraction depending on the temperature (the lower the temperature, the higher the superfluid fraction). A consequence of the inviscid nature of the superfluid component is that turbulent eddies cannot have arbitrary circulation: only vortices carrying a single quantum  $\kappa$  of circulation may

---

<sup>\*</sup>bernard.rousset@cea.fr

exist, the so-called quantum vortices [1]. Those vortices act as defects where the excitations from the normal component may scatter. This mechanism produces a transfer of momentum between the two components of He II, leading to a mechanical coupling called mutual friction.

At finite temperature and in absence of a temperature gradient, it is believed that this mutual friction locks the velocity fields of the two components at scales larger than the typical intervortex distance  $\delta$ . This explains the lack of observed difference in energy spectra on the large scale [2,3]. At scales comparable to  $\delta$ , it is predicted that mutual friction is not strong enough to lock the two components together, so a different behavior compared with classical turbulence is predicted [4]. The intervortex distance is expected to be of the same order of magnitude as the dissipative scale in the normal component, which may be very small in laboratory experiments (typically ranging between one and several tens of micrometers).

Since Eulerian sensors are difficult to use in He II and do not even exist on scales of less than a tenth of a millimeter, the use of visualization to probe the flow has been explored in the past decades [5,6] as a promising approach to access quantitative multiscale diagnosis of quantum turbulence.

$H_2$ - $D_2$  ice particles and hollow glass spheres have initially been used to assess the flow field in counter-flow experiments [7–10]. Those reveal that Lagrangian statistics at small scales appear to behave differently from those of the conventional fluid [11,12]. Nevertheless, due to the nature of the counter-flow itself (which has no counterpart in classical fluid), and also to the small level of turbulence involved in this situation, no clear conclusion has emerged yet regarding possible intrinsic differences in the dynamics of super- and normal-fluid turbulence when driven in similar conditions.

More recently, particle tracking velocimetry (PTV) has also been used to measure statistical properties of inertially driven flows. Svancara and La Mantia [13] used  $H_2$ - $D_2$  ice particles to look at velocity and acceleration probability density functions in an oscillating grid experiment. They found that the velocity and acceleration distributions were comparable to that observed in standard fluids, as already observed in Eulerian framework for scales larger than  $\delta$ . Tang *et al.* [14] studied the velocity structure functions scalings in a towed-grid experiment, in He II only. They conclude, among other things, that they observe a larger intermittency than in classical fluids on the basis of comparison with theoretical models.

It remains unclear at the moment which component the Lagrangian particles actually trace in He II (see, e.g., Ref. [15]). One goal of the present study is to proceed to different estimates of energy across scales in order to explore possible deviations from classical behavior, which may indicate any specificity of superfluid behavior (due either to a preferential sampling of the tracer to one component or the other, or to the existence of different channels for energy to flow and dissipate across scales). To this end, we have estimated the energy rates at different scales, always assuming fundamental laws as they are known for classical fluid turbulence, seeking scale by scale for significant differences between measurements carried in He I and He II. This direct comparison is the most reliable way to highlight features peculiar to He II.

To achieve this, we designed a new experimental facility devoted to particle tracking and particle trapping measurements in Oscillating Grid Turbulence [16] (OGT). The main difference with Svancara and La Mantia [13] is that we chose to follow the design rules of a canonical oscillating grid experiments, e.g., grid solidity below 40% and at least  $3 \times 3$  meshes with a half mesh at each end [17–19]. Thereby our experiment offers the possibility of calibrating and validating our measurements in He I against classical reference data. Compared with grid-generated turbulence in wind tunnels, OGT has the advantage to produce a flow with almost no mean flow and hence is better suited to particle tracking experiments with fixed cameras. Towed grid experiments, which are now common tools to investigate inertially driven turbulence [14,20,21], produce nearly homogeneous isotropic turbulence (HIT hereafter) that decays (nonstationary) in time. The choice of OGT for the present study was therefore motivated by its stationarity. It is an important condition because it ensures that the energy-injection rate, the energy transfer across scales, and the energy-dissipation rate should be equal.

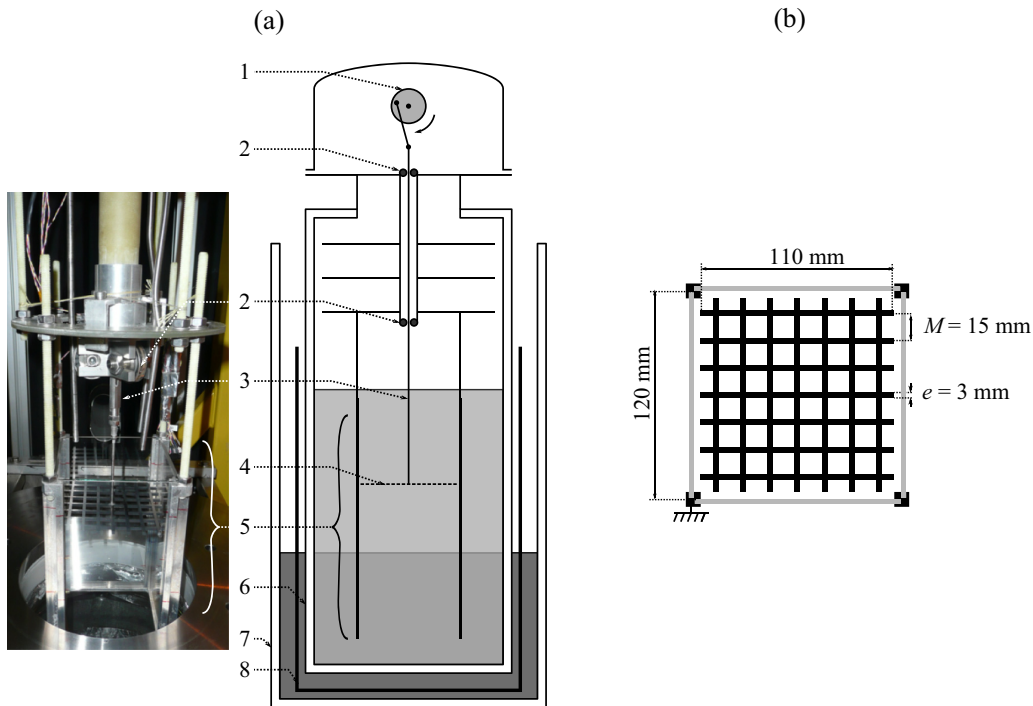


FIG. 1. (a) Experimental setup: (1) crankshaft + gear-motor system, (2) ball bearing, (3) composite main shaft, (4) grid, (5) test section (“aquarium”), (6) inner (helium) double-wall glass vessel, (7) outer (nitrogen) double-wall glass vessel, (8) Aluminum radiation shield. (b) Details of the grid and test section dimensions.

To have good control of particle size dispersion, we decided to use hollow glass microspheres. Such particles have a diameter of a few tens of micrometers (an order of magnitude bigger than ice particles) and part of our study aims at probing whether such particles would make good tracers.

In Sec. II we present the experimental device. Section III describes the typical experimental protocol to optimize the operation of the facility for particle-tracking measurements. Section IV A describes particle detection methodology before the exploration of particle trapping in Sec. IV B. Section IV C is dedicated to particle tracking. Finally, we present the velocity field in Sec. V and Sec. VI is devoted to the assessment of the dissipation rate at different scales of the flow.

## II. EXPERIMENTAL SETUP

To generate inertially driven turbulence in liquid helium, we designed an oscillating grid experiment together with a dedicated cryostat. The final scope is to access Lagrangian velocity statistics by means of particle-tracking experiments in He I and He II and also to investigate eventual preferential concentrations of particles in He II.

Figure 1(a) presents a simplified sketch view of the experiment with the main elements of the facility.

In the following we first detail the turbulence generation system, then describe the cryostat and the visualization setup, and finally describe the particle seeding technique.

TABLE I. Grid characteristics: mesh size  $M$ , grid bar thickness  $e$ , solidity  $G$ , frequency  $f$ , stroke  $S$ .

		Grid		
$M$	$e$	$G$	$f$	$S$
[mm]	[mm]	[%]	[Hz]	[mm]
15	3	36	5	26

### A. Turbulence generation

Turbulence is produced by oscillating a grid [item (4) in Fig. 1(a)] in a liquid helium bath (light gray). The grid is driven by a gear motor (1), inside the cryostat but at room temperature, via a shaft (3) which is designed to minimize heat losses due the thermal gradient.

The motor is a MDP EC40 equipped with a planetary gear head GP 42 C with a reduction ratio of 26 : 1. The system has a maximal rotation frequency of 6.4 Hz and can deliver a maximal torque of 4.2 N m. During the experiments presented in this paper, the grid was always driven at constant frequency  $f = 5\text{Hz}$ .

We use a crankshaft with an adjustable stroke  $S$  to convert the rotation to quasisinusoidal vertical translation. The maximal stroke is about 30 mm, but experiments exposed in this paper were all performed with  $S = 1.77M \approx 26\text{ mm}$ .

The grid oscillates vertically in a glass box [item 5 in Fig. 1(a)] with square cross-section immersed in the bulk of the liquid helium. The sides of the box are  $W = 120\text{ mm}$  large [marginally larger than the grid itself, see Fig. 1(b)] and the height is  $H = 250\text{ mm}$ . The top and bottom ends of the box are open: the goal of this ‘‘aquarium’’ is to ensure a reproducible turbulence generation region, with well-controlled boundary conditions. The open top and bottom help in minimizing recirculating flows, although some residual large-scale mean recirculations are known to be hardly avoidable in oscillating grid experiments. The four side walls of the aquarium are made of glass for optical access purposes.

#### 1. Grid Geometry

Figure 1(b) shows the grid geometry. It has been designed based on previous studies in classical fluids in order to respect canonical conditions on the solidity and the end conditions [18], known to produce a well-characterized turbulence, with good homogeneity and isotropy properties.

The grid is made of anodized aluminum with square bars and has a solidity  $G \approx 36\%$ . As a reminder, the solidity  $G$  is defined as the ratio between the frontal area effectively blocked by the bars and the total cross section area of the grid, which for a square grid as ours can be simply related to the bar width  $e$  and the mesh size  $M$ :

$$G = \frac{e}{M} \left( 2 - \frac{e}{M} \right). \quad (1)$$

When the grid solidity exceeds 40%, the jets and wakes produced by the oscillation of the grid are known to become unstable and merge together to form larger structures [17]. We have chosen a solidity of 36% ( $e = 3\text{ mm}$ ,  $M = 15\text{ mm}$ ) for which ‘‘ the wakes coalesce with each other without bending their axes; shear-free turbulence can be expected on either side of the grid at sufficiently large  $z$ ’’ [22].

Table I summarizes the grid characteristics.

#### 2. Expected flow characteristics

From the chosen grid parameters, it is possible to estimate the expected flow characteristics by means of empirical laws. The integral length scale  $L$  increases linearly with the distance to the

TABLE II. Expected flow characteristics. (a) Primary quantities obtained from correlations (2) and (3) at  $f = 5 \text{ Hz}$ ,  $\frac{S}{M} = 1.77$ ,  $\frac{z}{M} = 4.6$ . The main assumption is that the energy injection at large scale does not depend on the fluid. The uncertainties are computed by considering the minimum and maximum values of  $z$  in the field of view together with reported uncertainties on  $c_L$  and  $c_u$ . (b) Derived quantities:  $\epsilon$  from Eq. (4),  $Re_\lambda$  is the Reynolds number based on the Taylor length and is obtained under the assumption of homogeneity and isotropy of the flow as  $Re_\lambda = \sqrt{15}L\sigma_u/\nu$ ,  $\eta$  is the Kolmogorov length scale, and  $\tau_\eta$  is the Kolmogorov timescale. In He II, we define the kinematic viscosity as  $\nu = \mu_n/\rho$ , where  $\mu_n$  is the dynamic viscosity of the normal component and  $\rho$  is the total density.

		$L$ [mm]	$\sigma_u$ [mm s <sup>-1</sup> ]			
	(a)	$14 \pm 5$	$9.3^{+2.6}_{-1.9}$			
$T$ [K]	$P$ [bar]	$\epsilon$ [ $1 \times 10^{-5} \text{ m}^2 \text{ s}^{-3}$ ]		$Re_\lambda$	$\eta$ [ $\mu\text{m}$ ]	$\tau_\eta$ [ms]
(b)	2.8	1	$5.8^{+12.2}_{-3.7}$	280	22	20
	3.5	1	$5.8^{+12.2}_{-3.7}$	270	24	21
	2	0.031 (sat.)	$5.8^{+12.2}_{-3.7}$	440	11	10

grid  $z$ :

$$L = c_L z, \quad (2)$$

where  $c_L$  is a constant that depends on the grid geometry. For comparison we will use  $c_L = 0.2$ , which is the value Hopfinger and Toly [17] obtained with  $S/M = 8/5$ , the closest to our configuration.

For simplicity, we define the origin of the vertical coordinate  $z$  as the midpoint of the oscillation even though Hopfinger and Toly [17] report virtual origins of order  $M$ .

The transverse (horizontal) fluctuating velocity  $\sigma_u$  has been shown to follow

$$\sigma_u = c_u f M^{1/2} S^{3/2} z^{-1}, \quad (3)$$

where  $c_u$  is a constant that depends on the grid geometry. Based on the literature [17,22] we consider  $c_u = 0.25$ . The fluctuating velocity decreases as the inverse of the distance  $z$ .

In the sequel we also measure the dissipation rate  $\epsilon$  per unit mass of the flow. In previous grid experiments, it has been shown to behave as

$$\epsilon = C_\epsilon \frac{\sigma_u^3}{L}, \quad (4)$$

where  $C_\epsilon \approx 1$  [23].

Assuming that the flow is quasihomogeneous and isotropic, from the dissipation rate one can then infer the Kolmogorov dissipative length scale

$$\eta = \left( \frac{\nu^3}{\epsilon} \right)^{1/4}. \quad (5)$$

It is generally unclear how exactly the kinematic viscosity  $\nu$  should be defined in He II flows. Babuin *et al.* [24] have measured an effective viscosity  $\nu_{\text{eff}}$ , which is defined as the ratio between the dissipation rate and the mean enstrophy in a turbulent grid flow. They found that, around 2 K, the value of  $\nu_{\text{eff}}$  is of the same order of magnitude as  $\mu_n/\rho$ , where  $\mu_n$  is the dynamic viscosity of the normal component. In the sequel, we thus use  $\nu = \mu_n/\rho \approx 1 \times 10^{-8} \text{ m}^2 \text{ s}^{-1}$  as an approximation in He II.

Table II summarizes the above primary and derived quantities in our experimental conditions.

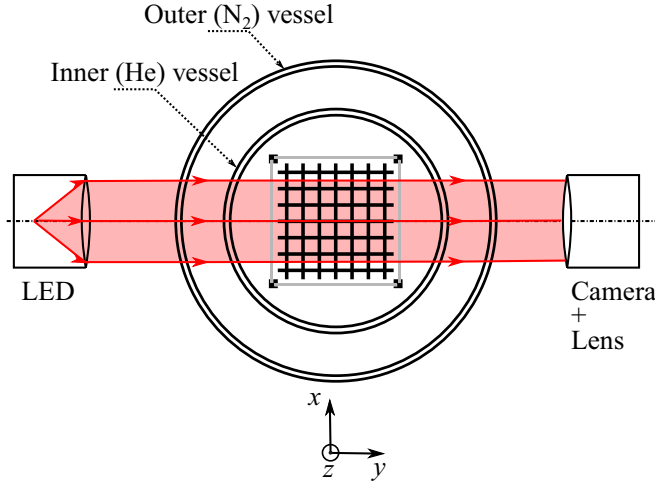


FIG. 2. Top view of visualization system.

### B. Cryostats

Usually, visualization experiments in cryogenic facilities are performed in stainless-steel cryostats with small planar optical accesses to minimize heat losses in the helium bath [9,11,25]. However, the field of view is then limited by the number of available windows and by the diameter of the windows. We have chosen for our facility to use glass (rather than stainless steel) as the material for the cryostat in order to have a higher level of versatility for visualization purposes. For instance, although we only present here two-dimensional (2D) measurements, a glass cryostat with full optical access allows us to consider in future campaigns multicamera experiments for simultaneous recordings at several viewing angles, hence allowing well-resolved three-dimensional (3D) particle-tracking measurements. The use of a glass cryostat has the additional benefit of being less expensive than the mixed stainless-steel plus glass solution because it avoids the requirement of sophisticated welding between a stainless-steel cryostat and optical accesses.

Two cylindrical concentric double-wall glass vacuum cryostats are used. The inner cryostat contains the liquid helium bath, where the turbulence is generated. The outer cryostat contains liquid nitrogen and plays the role of thermal shield to limit losses between room temperature and the bulk of liquid helium. Glass is naturally opaque to the infrared radiations and is heated by room-temperature radiation and in turn heats up the liquid nitrogen, thus producing bubbles. These bubbles disturb the visualization through the cryostats. To avoid this perturbation, the level of nitrogen is kept below the visualization area during operation of the experiment. This in turn reduces the efficiency of the nitrogen thermal shield. To further minimize radiation heat load, an aluminum shield [item 8 in Fig. 1(a)] is also immersed inside the liquid nitrogen cryostat. Holes are made in the aluminum shield at the level of the visualization area. Note that this aluminum shield is disposable and a new adapted shield can easily be prepared if cameras are added to the experiment or if the visualization area needs to be enlarged.

### C. Visualization system

Measurements are based on high-speed visualization with a Phantom V12 camera (with a maximum frame rate of 6200 images per second at the highest resolution of 1280 pixels  $\times$  800 pixels on a one inch CMOS sensor). We use a red light-emitting diode (LED) with a collimation lens in order to produce an approximately parallel light beam aiming straight on the camera lens, as shown in Fig. 2.

TABLE III. Particles characteristics: mean diameter  $\Phi_p$ , mean density  $\rho_p$ .

Material	$\Phi_p$ [ $\mu\text{m}$ ]	$\rho_p$ [ $\text{kg m}^{-3}$ ]
Hollow glass	$85 \pm 15$	$177 \pm 45$

In this backlight configuration, we record the shadows of the particles traveling across the light beam, with an a priori undetermined position in the  $y$  direction (along the line of sight of the camera). We therefore use a lens with a large numerical aperture (a long-distance microscope K2-SC CF-1/B) that ensures both a good luminosity (and contrast) and a small depth of field. The latter has been measured to be of the order of  $\delta_{\text{dof}} \simeq 1.4$  mm, hence ensuring quasi-2D measurements at a fixed known  $y$  position. Besides, the backlight configuration allows for a good contrast with a low light power, which minimizes the heat sources into the helium bath.

All the measurements discussed here have been done at a vertical position centered around a distance  $z = 4.6M$  below the average position of the grid. The overall field of view is  $1.8M \times 1.2M$  (i.e.,  $25 \times 18$  mm<sup>2</sup>). The camera lens was located at a working distance of 35.5 cm from the center of the aquarium. The geometrical configuration is the same in He I and in He II.

#### D. Particles

Particle seeding was done by using K20-type hollow glass microspheres from 3M. These particles are commercially available as a polydisperse population with sizes ranging from 10 to 200  $\mu\text{m}$  and densities ranging from 130 to 200  $\text{kg m}^{-3}$ .

We first sieved the particles in order to remove the largest and smallest ones. Only particles that have a diameter larger than 71  $\mu\text{m}$  and smaller than 100  $\mu\text{m}$  have been retained for our measurements. The particle size distribution has then been measured using a Spraytech diffractometer from Malvern Instruments, Ltd. The particle mean diameter D32 (defined as the ratio between the mean volume and the mean area) has been found to be of the order of 85  $\mu\text{m}$ .

We also measured the average particle density: we immersed a known mass of particles in a known volume of water and measured the resulting total volume. We found a mean particle density of the order of 177  $\text{kg.m}^{-3}$ .

Table III summarizes the particle characteristics.

Finally, we observed the shape of the particles with a binocular and verified that they were spherical except for a small fraction corresponding to broken particles. These pieces of sphere were no longer hollow and contributed to a slight increase in overall density so that the value of 177  $\text{kg.m}^{-3}$  is a maximum value. During the experiment, the broken particles sank rapidly after injection.

Particles are dried and injected in the flow using a removable cryogenic syringe. A few minutes before recording data, we start oscillating the grid. This has two main advantages: (i) the flow reaches a steady state and (ii) dense or broken hollow microspheres settle and only particles with a density close to the density of the fluid stay in our visualization field. Typically we estimate that the difference between particles density and fluid density to be less than 15%.

### III. EXPERIMENTAL PROCEDURE

As mentioned in the introduction, we aim at performing experiments both in normal He I and superfluid He II. From a cryogenic point of view, a fundamental difference between these two states of liquid helium concerns the heat conductivity. While He I has a very low thermal conductivity (e.g., 0.02  $\text{W m}^{-1}\text{K}^{-1}$  at 3 K and 1 bar), He II has a very high effective thermal conductivity. As a consequence, a He II bath is quasi isothermal, as opposed to a He I bath.

TABLE IV. Experimental conditions: temperature  $T$ , density  $\rho_f$  of the carrier fluid, oscillating frequency  $f$  of the grid.

Config. #	Fluid	$T$ [K]	$\rho_f$ [kg m <sup>-3</sup> ]	$f$ [Hz]
1	He I	$2.8 \pm 0.1$	145.0	5
2	He I	$3.5 \pm 0.1$	138.0	5
3	He II	2	147.5	5

If the free surface of liquid helium is at saturation pressure  $P_{\text{sat}}(T_{\text{free-surf}})$ , in absence of a temperature gradient in the fluid, any point below the free surface is subcooled due to the pressurization resulting from the immersion depth. In He II it is reasonable to assume that there is no temperature gradient and the liquid is therefore always subcooled. This ensures that no bubbles appear and perturb the flow.

On the contrary, He I has a low thermal conductivity and the temperature of the liquid below the free surface can increase due to parasitic heat inputs (through the walls). Those temperature differences can easily overcome the subcooling due to the immersion depth, resulting in boiling inside the bath.

To avoid the presence of bubbles in the field of view, the following procedure is applied for He I experiments: After filling with liquid helium, the bath is cooled down to 2.4 K by pumping, the liquid level being kept well above the top of the test section. Then, helium gas at atmospheric pressure is reintroduced above the liquid interface enabling pressurization and stratification (cold liquid is denser and remains at the bottom). This pressurization process gives enough time to perform quasistationary measurements in He I without bubbles: we can typically have half an hour at the operating grid frequency (5 Hz) before the temperature at the visualization level reaches the saturation temperature ( $\approx 4.2$  K), generating bubbles again.

In He II, a MKS 600 valve is used to control the bath pressure (hence the temperature). As previously mentioned, the grid is oscillated a few minutes before taking measurements in order to ensure a steady state is reached [26]. For the three explored experimental conditions (see Table IV), at least 80 films of 400 images are recorded to achieve a good statistical convergence. To resolve particle dynamics, the sequences of 400 images are recorded at a frame rate  $F_s = 3000$  frames per second so that  $\delta t \ll \tau_\eta$ , where  $\tau_\eta$  is the dissipative Kolmogorov timescale of the flow (previously estimated in Table II) and  $\delta t = F_s^{-1}$  is the time between two images. Typically we have 60 frames per  $\tau_\eta$ .

Furthermore, images extracted from different films can be considered as uncorrelated because the delay between two consecutive films is 20 s, which is greater than the integral time of the flow (1.4 s).

The different test conditions explored in this paper consist in three different configurations that are summarized in Table IV.

#### IV. IMAGE PROCESSING

In this section we first describe how the image sequences are postprocessed to determine the position of individual particles at a given time  $t$ . The seeding procedure is then validated using Voronoï tessellation to show that particles are randomly distributed in space. Finally, we show how we reconstruct tagged particle tracks along time from individual particle positions.

##### A. Particle detection

Figure 3 shows a typical raw image of the hollow microspheres to be tracked in the oscillating grid flow. This image shows important optical distortions which may affect particle detection and

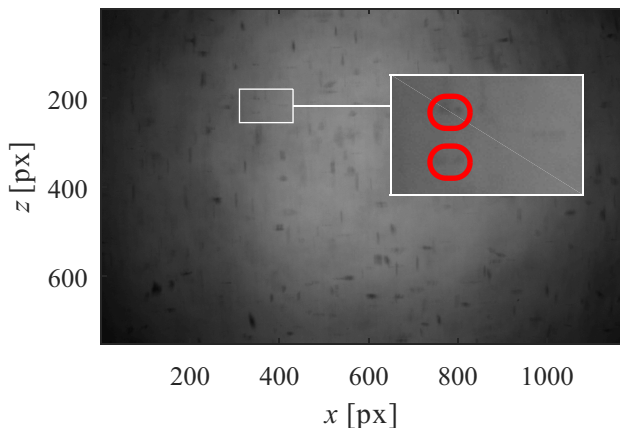


FIG. 3. Raw image with a zoom on ghost particles in He II at 2 K (Config. #3, see Table IV). The field of view is  $1280 \text{ px} \times 800 \text{ px}$ .

eventually the accuracy of the overall particle-tracking procedure. It can indeed be seen that out-of-focus particles are strongly distorted, with either a vertical or a horizontal image. This anisotropic distortion is classical of a cylindrical lens effect, very likely induced by the cylindrical double walls of the inner and outer cryostats. The main goal of the image postprocessing is to correctly detect the particles which are in focus.

The overall image processing sequence is as follows: First, to clean images, we apply morphological opening of the image in order to retrieve the slightly inhomogeneous background illumination, which is subtracted from the corresponding image. Second, a thresholding is applied to select the most contrasted particles; this eliminates most particles that are out of the depth field because they are dimmer. Finally, in-focus particles are often found to exhibit a pattern with multiple (typically three) images closely aligned in the horizontal direction. This is very likely due to multiple reflections between the walls of the concentric cryostats. To remove this effect, a morphological closing using a small horizontal segment is used to connect dark pixels (we recall that particles appear dark on a bright background) that are closer to each other by less than five pixels (i.e.,  $100 \mu\text{m}$ ). This leads to processed images where most in-focus particles appear as smooth blobs of pixels. Their center is determined as the center of mass of these blobs, see Fig. 4.

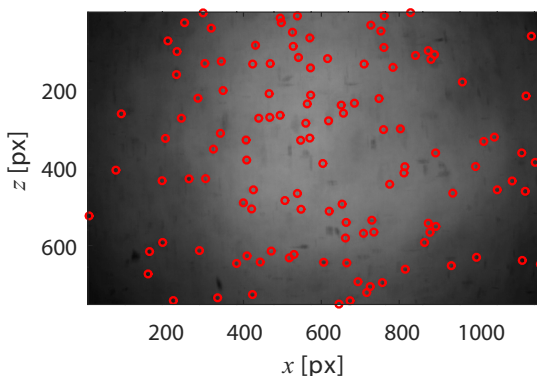


FIG. 4. Detection of particles in the raw image from Fig. 3, in He II at 2 K (Config. #3, see Table IV).

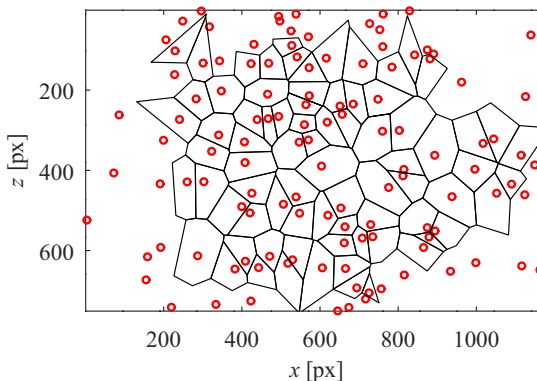


FIG. 5. Voronoi diagram of particles detected in Fig. 4, in He II at 2 K (Config. #3, see Table IV).

### B. Seeding validation procedure

The flow conditions explored here lead to a Kolmogorov scale (in He I) of the order of  $23 \mu\text{m}$ . According to Babuin *et al.* [24], we expect that the intervortex distance should be of the same order. Thus, the  $85 \mu\text{m}$  microspheres used here are also of the same order of magnitude. In addition, the microspheres that remain in the field of view after a certain delay have a density very close to the density of the fluid. These particles can therefore be expected to behave like tracers and be randomly distributed in space. In this section, we will verify this in both He I and He II.

Contrary to ideal tracers, which follow the flow and are randomly distributed, inertial particles may experience clustering (see, e.g., Monchaux [27]). On the other hand, even for tracer particles, preferential concentration may arise in He II due to the trapping of particles about the core of the quantized vortices. This phenomenon has been widely studied by direct visualization of turbulent counter-flow experiments [10,28,29] in He II at rest, but has never been addressed in mechanically forced superfluid turbulence.

Following Monchaux *et al.* [30], we propose to explore the seeding properties based on Voronoi tessellations of the spatial distribution of the detected particle centers in order to explore whether particles exhibit some nontrivial structure. We thus use a Voronoi diagnosis in a superfluid experiment. Note that we do not aim here to explore in detail the possible trapping of particles by quantized vortices, a topic which goes beyond the scope of this article, but simply to check whether the particle distribution is random or exhibits some significant degree of preferential concentration. The presence of clustering of particles would reveal a possible bias in the subsequent analysis of particle dynamics due a trapping mechanism. The absence of clustering, even though reassuring, cannot totally rule out a possible bias because it is unclear how the distribution of particles preferentially trapped by randomly entangled vortices should look. This is a very interesting topic which deserves a dedicated study. We consider, however, that, in the absence of significant differences in the seeding properties diagnosed by Voronoi tessellation between normal and superfluid conditions, no major bias due to trapping is expected.

A Voronoi diagram consists in defining a cell that contains all the points of the space that are closer to a given particle than to any other particle. Such a cell, associated with a particle  $i$  appearing on a frame at time  $t$  has an area  $A_i(t)$ . Figure 5 presents the Voronoi diagram of particles detected in Fig. 4.

In regions with a large number of particles, Voronoi cells have a small area, and where there are few particles, cells are bigger. Experimentally, we observe that the number of particles per frame decreases with time (settling due to the slight density mismatch), although the overall average spatial distribution of particles within the measurement zone does not exhibit any large-scale inhomogeneity. Consequently, we measure the normalized area  $\mathcal{A}_i(t) = A_i(t)/\bar{A}_i^t$  where  $\bar{A}_i^t$  stands

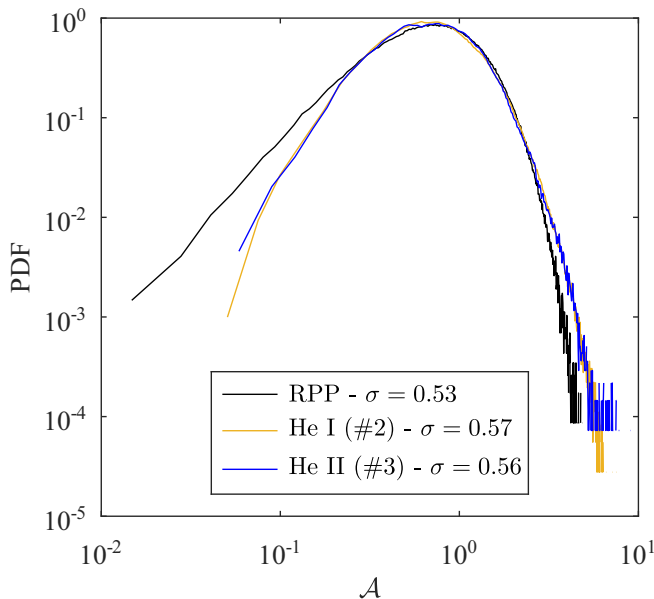


FIG. 6. Probability density functions of normalized Voronoï area  $\mathcal{A}$ .

for the average of  $A_i(t)$  measured at time  $t$ . The cell area's probability density function (PDF) provides a quantitative way to describe the degree of clustering of a set of particles. This method of analysis of particle preferential concentration has already been widely used but we use it on He II seeding. We applied this method to our measurements both in He I and He II.

In Fig. 6, the black curve represents the PDF of the Voronoï cell areas in the case of randomly distributed particles. This kind of distribution can be modeled by a random Poisson process (RPP) for which the standard deviation of Voronoï cell areas can be analytically calculated as  $\sigma \approx 0.53$  [31]. The blue and orange curves are the PDF of Voronoï areas in He I and He II, respectively. The curves follow the same trend within the accuracy of our measurements. Therefore, the spatial distribution of particles does not depend on the state of helium. Furthermore, in spite of some small deviations in the tails of the measured distributions compared with RPP case (note, however, that the deviations appear amplified by the logarithmic scale), the PDF in He I and He II both have a standard deviation  $\sigma$  comparable to that of the RPP. This means that the distribution of the particles is very close to random, as expected for tracer particles.

We have done further tests that show that the PDF do not depend on the height  $z$ , either. This demonstrates that the position of the injector is sufficiently far to avoid any residual preferential concentration.

At this point, it is interesting to have an estimate of the intervortex distance  $\delta$ . The latter can be obtained, following Babuin *et al.* [24], from the turbulent Reynolds number computed using an effective  $\nu_{\text{eff}} \approx \kappa/5$ . This leads to  $\delta \approx 35 \mu\text{m}$ .

Consequently, we should consider that a single particle is always in contact with at least two vortices. In that case, it is difficult to predict the effect of the trapping mechanism on our “big” particle. Nevertheless, our data show no significant deviation from a homogeneous distribution.

### C. Particle tracking

Once particles are identified (typically we have an average of 80 particles per image), they are tracked to get their trajectory along time. For this we perform Lagrangian particle tracking using the particle tracking code by Ouellette [32].

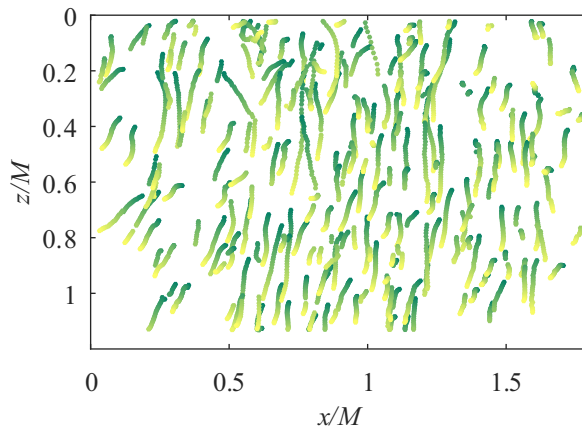


FIG. 7. Particle trajectories over 400 images in He II (Config. #3 in Table IV). Dark green is for  $t = 0$  and light green relates to the end of a video (400th image) at  $t = 133$  ms.

In Fig. 7, we show typical trajectories obtained after particle tracking over a sequence of 400 images acquired at a frame rate of 3 kHz.

Lagrangian velocity and acceleration are obtained by convolution of the raw trajectories with a truncated Gaussian smoothing and differentiating kernel [33] to filter high-frequency noise from the recorded trajectories. Traditionally, the width of the filtering kernel is chosen to minimize the impact of noise on acceleration variance [34–37]. However, the level of small-scale noise is particularly high in our experiment compared with classical experiments at ambient temperature, due to the multiple curved optical interfaces between the core of the cryostat and the cameras. As a consequence, the typical timescales of the noise overlap with the small turbulent dynamics of the particles, and estimates of acceleration remain sensitive to the choice of the filtering width, which affects the robustness of acceleration statistics (see Sec. VIC). Future experiments are planned to improve this by an entirely new design of the cryostat in order to avoid multiple layers of curved interfaces. For the present study, we therefore chose the filtering properties based on particle velocity variance, which is less sensitive to small-scale noise than acceleration. We find that a Gaussian smoothing kernel of width 6 ms (18 frames) limits reasonably well the impact of noise with a weak impact on velocity estimates.

Figure 8 represents an example of such a raw and filtered trajectory, clearly showing the high degree of small-scale noise. As discussed in Sec. VB, even after this filtering procedure, velocity increment statistics at inertial scales may still be weakly affected by some remaining level of noise. This led us to deploy a strategy in order to access a robust statistical estimate of the Lagrangian dynamics of the particles based only on their position (and position increments) statistics, hence avoiding the amplification of noise associated with numerical differentiation (see Secs. VB and VIB 1).

## V. SINGLE-TIME VELOCITY STATISTICS

Figure 7 shows a typical set of reconstructed trajectories. An overall vertical trend of particle motion can be seen which suggest the existence of a mean drift velocity, see Refs. [26,38]. This is expected as particles are slightly denser than the carrier fluid, see Table V. Besides, to get a zero mean velocity in an oscillating grid experiment, an infinite aspect ratio of the aquarium for the test section  $H/W$  is required. In the horizontal direction, where the gravity should have no effect, the mean velocity  $\langle u \rangle$  has been measured and found to be negligible compared with velocity fluctuations. The ratio between the average and the standard deviation of the velocity is  $\langle u \rangle / \sigma_u \approx 0.1$

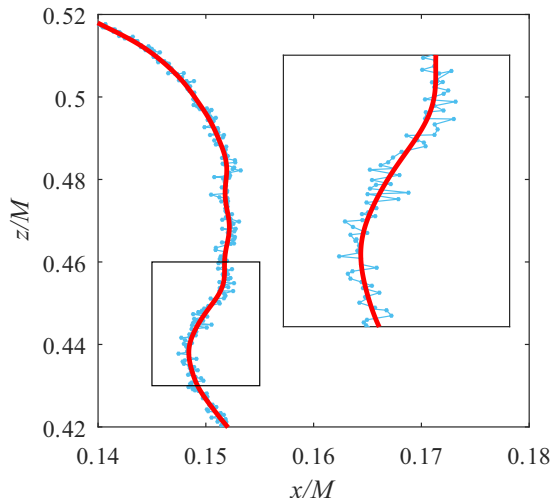


FIG. 8. Particle trajectory filtered with a Gaussian kernel of width 18 points (6 ms).

in He I and  $\langle u \rangle / \sigma_u \approx 0.3$  in He II. In the next sections we focus the analysis on the horizontal component  $u$  of the velocity.

#### A. Velocity probability density function and classical fluctuating velocity computation

Figure 9 shows the centered and reduced probability density function (PDF) of the horizontal velocity fluctuations. They are found to be quasi-Gaussian, with slightly over-Gaussian tails. Surprisingly, the PDF of velocity fluctuations is not well documented in the existing literature of oscillating grid turbulence in classical fluids. One exception is the thesis of Drayton [39], who reports that, for measurements performed further than about four meshes from the grid, (i) velocity PDFs do not exhibit any significant asymmetry, (ii) they are nearly Gaussian up to about two standard deviations, and (iii) they present over-Gaussian tails beyond typically two-standard deviations. These trends are in very good qualitative agreement with the PDFs we report in Fig. 9, both in He I and He II conditions. Therefore, no visible deviation of inertially forced superfluid turbulence from the classical behavior is detectable in these PDFs. In particular, we do not observe the emergence  $u^3$  tails as has been reported in superfluid counter-flows.

The PDFs shown in Fig. 9 were reduced by the velocity standard deviation in order to explore first any eventual change of the global shape of the fluctuations distribution between the normal and the superfluid cases. Because no significant such change has been observed, we focus now on the velocity standard deviation of velocity fluctuations itself. Table V summarizes the trends of the standard deviation of velocity and its comparison with the expected value from classical empirical laws usually used for oscillating grids in classical fluids [Eq. (3)]. A good agreement is found with

TABLE V. Summary of horizontal velocity measurements obtained using position differentiation.

Config.	Fluid	$\sigma_u$ [mm s <sup>-1</sup> ]	$\langle u \rangle$ [mm s <sup>-1</sup> ]	$\frac{\sigma_u}{\sigma_u^H}$
1	He I	$8.3 \pm 1.7$	0.9	0.86
2	He I	$9.3 \pm 1.9$	0.3	0.96
3	He II	$9.1 \pm 1.8$	-3.2	0.94

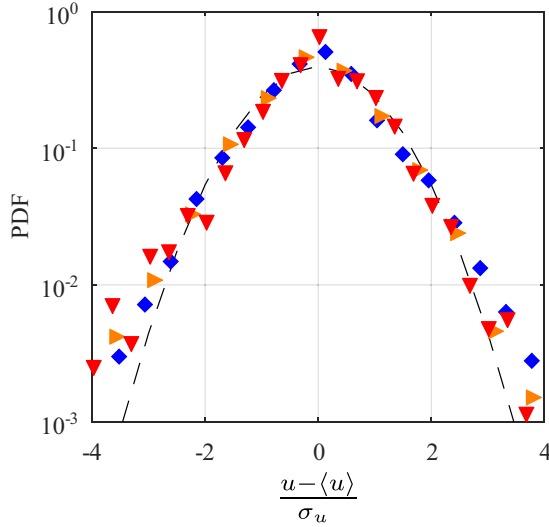


FIG. 9. Probability density function of normalized velocities alongside the horizontal axis  $x$ .  $\blacktriangledown$  He I (#1),  $\blacktriangleright$  He I (#2),  $\blacklozenge$  He II (#3).

the empirical law, with no major difference between the fluid and the superfluid cases. A small difference is observed however between the two measurements performed in He I: Config. #1 shows a larger deviation from empirical laws.

### B. An alternative way to access the fluctuating velocity

Lagrangian velocity is usually obtained from the derivative of individual particle trajectories (see previous Sec. V A). Statistics are then estimated from this data set of individual velocities. Such a numerical differentiation process on individual trajectories tends to amplify the noise present in the position data of the particles and requires to filter the trajectories. As described in Sec. V A, this is done here using Gaussian-filtering. Choosing appropriate filtering parameters is not trivial: if individual trajectories are not sufficiently filtered, the statistical quantities estimated (as the velocity standard deviation) may be biased because they still include noise contributions, whereas if the trajectories are too filtered, they will be artificially smoothed.

We propose here an alternative estimation of the standard deviation of the particle velocity based on purely kinematic considerations of the position temporal increments  $\delta x$ . This approach does not require filtering individual trajectories and hence gives a more robust estimate. It is described in more detail by Machicoane *et al.* [40].

Let us consider the mean square displacement of the particles  $\delta x^2 = \langle (x(t) - x(t + \tau))^2 \rangle$  where  $x(t)$  and  $x(t + \tau)$  represent the horizontal position at two different times of the same particles along its trajectory. Assuming the trajectories are smooth (and differentiable) for sufficiently small time lags while they become uncorrelated and nonsmooth for large time lags, the mean square displacement is expected to have at least two asymptotic regimes:

$$\langle \delta x^2 \rangle = \begin{cases} u_{\text{rms}}^2 \tau^2 & \text{for } \tau \ll T_L \\ 2u_{\text{rms}}^2 T_L \tau & \text{for } \tau \gg T_L, \end{cases} \quad (6)$$

where  $u_{\text{rms}}^2$  is the second-order moment of the velocity and  $T_L$  represents the Lagrangian correlation timescale of the particles motion. In our study the duration of a video (133 ms) is shorter than the integral time  $T_L = 1.4$  s, so only the short-term ballistic regime  $\langle \delta x^2 \rangle = u_{\text{rms}}^2 \tau^2$  is expected to be observed.

In practice, experimental data of particle position do not exhibit a smooth ballistic regime at the smallest timescales, because of the presence of experimental noise. This results in a deviation from the quadratic dependence  $\delta x^2 \propto \tau^2$  for the smallest  $\tau$ . For a purely uncorrelated noise, mimicking perfect Brownian motion at short timescales, one would expect to see  $\delta x^2 \propto \tau$ . To model the influence of noise, the measured particle position  $x$  can be written as the sum of the real position  $x^*$  (without noise contribution) and the experimental noise  $\theta$ :  $x = x^* + \theta$ . The measured mean square displacement can then be rewritten, for the short time lags, as

$$\langle \delta x^2 \rangle = u_{\text{rms}}^2 \tau^2 + 2\langle \theta^2 \rangle [1 - R_{\theta\theta}(\tau)] + O(\tau^3), \quad (7)$$

where  $R_{\theta\theta}$  is the autocorrelation function of the noise:

$$\lim_{\tau \rightarrow 0} R_{\theta\theta}(\tau) = 1, \quad (8)$$

$$R_{\theta\theta}(\tau \gg \tau_\theta) = 0. \quad (9)$$

Here  $\tau_\theta$  is the correlation timescale of the experimental noise.

From Eq. (7), by replacing  $u_{\text{rms}}^2$  by  $\langle u \rangle^2 + \sigma_u^2$ , hence not necessarily assuming the mean velocity  $\langle u \rangle$  is zero, one sees that the standard deviation of the velocity  $\sigma_u$  can be estimated from the measured mean square displacement:

$$\langle \delta x^2 \rangle - \langle u \rangle^2 \tau^2 = \sigma_u^2 \tau^2 + 2\langle \theta^2 \rangle [1 - R_{\theta\theta}(\tau)] + O(\tau^3). \quad (10)$$

If we consider time lags  $\tau$  sufficiently short to neglect high-order corrections to the ballistic term  $\sigma_u^2 \tau^2$  (what implies  $\tau \ll T_L$ ), although longer than the correlation timescale  $\tau_\theta$  of the noise in order to neglect  $R_{\theta\theta}$ , the velocity standard deviation can be robustly estimated from simple finite-time position increments (hence without effectively differentiating the trajectories) from the following relation:

$$\sigma_u^2 + 2 \frac{\langle \theta^2 \rangle}{\tau^2} = \frac{\langle \delta x^2 \rangle}{\tau^2} - \langle u \rangle^2, \quad (11)$$

for  $\tau_\theta \leq \tau \leq T_L$ .

Figure 10 presents  $(\langle \delta x^2 \rangle / \tau^2 - \langle u \rangle^2)^{1/2}$  as a function of  $\tau^2$ . The rapid initial decrease corresponds to the noise contribution  $2\theta^2/\tau^2$  and possibly also to some reminiscence of the noise correlation  $R_{\theta\theta}$ , which may not be exactly zero for the shortest time lags. We see, however, that the curve rapidly reaches a plateau, which suggests that the second term on the left-hand side of Eq. (11) is negligibly small and that the contribution of the noise to the position increment variance vanishes for a time lag corresponding to one or two inter-frame times.

At large timescales, the decrease of the curve corresponds to the onset of high-order corrections to the initial ballistic displacement, but probably also to statistical bias associated with the correlation between the duration of a track and the velocity of the corresponding particle: at large time, we essentially sample slow particles. We have no robust explanation though for the difference between the data sets with regards to the time at which the curves departs from a plateau. We therefore only focus on the time lapse for which the expected short-term ballistic regime appears well behaved.

The value of the plateau at intermediate timescales gives a robust estimate of the standard deviation of the velocity  $\sigma_u$ . These new estimates are reported in Table VI for both He I and He II experiments and compared with the estimates from the empirical laws for oscillating grid turbulence. It can be noted that this new estimate shows no significant difference between He I and He II. The agreement with the empirical laws is good, although the measured value is systematically of the order or 20% smaller than the empirical estimates. This difference can be attributed to a slightly different value of the constant  $c_u$  [see Eq. (3)] in our experiment compared with tabulated values in the literature. This may be the consequence of minor geometrical differences between our setup to the reference ones.

Note that the new estimates of  $\sigma_u$  are slightly lower than the direct estimate from Lagrangian velocity. This points to the fact that, in spite of the Gaussian filtering, taking the derivative of the

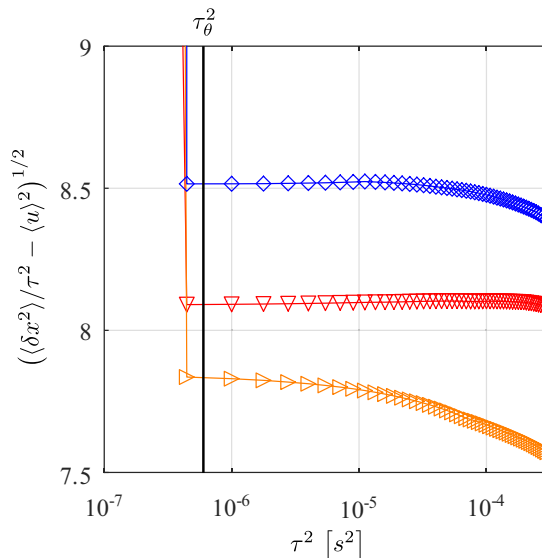


FIG. 10. Estimate of  $\sigma_u$  from the second-order moment of the separation along the horizontal axis  $x$  [see Eq. (11)] at  $f = 5$  Hz,  $\frac{S}{M} = 1.77$  and  $\frac{z}{M} = 4.6$ .  $\blacktriangledown$  He I (#1),  $\blacktriangleright$  He I (#2),  $\blacklozenge$  He II (#3). The difference in time between each point corresponds to the inter-frame time of the recorded movies.

position to estimate velocity remains a noise-amplifying operation. The excess of standard deviation measured from the velocity estimate is very likely due to a choice of filter width too narrow to efficiently reduce the noise.

## VI. ENERGY BUDGET

In this section we assess the estimate of the energy-injection rate  $\epsilon_L$ , the energy transfer  $\epsilon_l$  across inertial scales, and the dissipation rate  $\epsilon_\eta$ . The energy injection is estimated based on large-scale statistics, using the results of the previous section on velocity fluctuations. The energy-transfer rate is estimated at inertial scales of turbulence by using the second-order Eulerian structure function and classical Kolmogorov scalings. Finally, we show an attempt at determining the dissipation rate  $\epsilon_\eta$  based on Lagrangian acceleration measurements and the use of the Monin-Yaglom relation, which relates the dissipation rate  $\epsilon_\eta$  to the variance of acceleration.

In stationary conditions, in classical turbulence, the three estimates are expected to be identical because the only channel to dissipate energy is viscosity. All the injected energy therefore flows across scales via a unique cascade ending in viscous dissipation.

In He II, the question remains somehow open, since other dissipation mechanisms may exist which would lead to multiple channels for the energy to flow across scales in the normal and superfluid components which are eventually coupled via mutual friction [41].

TABLE VI. Summary of horizontal velocity measurements obtained using quadratic displacement fitting.

Config.	$T$ [K]	$\sigma_u$ [mm s $^{-1}$ ]	$\frac{\sigma_u}{\sigma_u^{\text{th}}}$
1	2.8	8.1	0.84
2	3.5	7.8	0.81
3	2	8.5	0.88

It remains unclear at the moment which component the Lagrangian particles actually trace in He II. One goal of the present study is to proceed to different estimates of energy across scales in order to explore possible deviations from classical behavior, which may indicate any specificity of superfluid behavior (due either to a preferential sampling of the tracer to one component or the other or to the existence of different channels for energy to flow and dissipate across scales). To this end, we have estimated the energy rates at different scales, always assuming fundamental laws because they are known for classical fluid turbulence, seeking scale by scale for significant differences between measurements carried out in He I and He II.

### A. Energy injection at large scales

Mechanical energy is injected into the flow at a scale  $L$ , known as the integral scale of the flow. A fundamental property of classical turbulence, related to the so-called dissipative anomaly property, relates the energy-injection rate  $\epsilon_L$  to the standard deviation  $\sigma_u$  of velocity fluctuations and to the integral scale  $L$  of the flow:  $\epsilon_L = C_\epsilon \sigma_u^3 / L$ .

$C_\epsilon$  is a universal constant of order unity [42]. In classical fluids, the dissipative anomaly stands for the fact that this relation does not involve viscosity, whereas all the energy which is injected at large scales is eventually dissipated at small scales by viscosity. This implies that dissipation remains finite even in the limit of vanishing viscosity, which in turns implies the appearance of ever smaller scales eventually leading to the energy cascade of turbulence.

We make use here of Eq. (4) to estimate the energy-injection rate. We assume the Reynolds number of our flow is large enough for  $C_\epsilon$  to be constant and take  $C_\epsilon = 1$ .

We cannot directly estimate at the moment the integral scale of our flow. This would imply measuring Eulerian statistics over a much larger measurement volume than what is currently accessible. We therefore estimate the integral scale based on the empirical law (2) for oscillating grids. This is justified due the relative good agreement already reported in the previous section for the fluctuating velocity compared with the corresponding empirical law. Besides, in Eq. (4), the dependency on  $L$  is linear, while the dependency on  $\sigma_u$  is cubic. We therefore expect that major impacts on the overall estimate of  $\epsilon_L$  will be associated with changes of  $\sigma_u$  rather than eventual small deviations of  $L$ .

Figure 11 shows the estimates of  $\epsilon_L$  for the three different experimental configurations we have explored. The gray area in Fig. 11 depicts the range of expected values for  $\epsilon$  in our experimental conditions, considering the main uncertainty which lies in the value of experimental constants as determined by earlier studies:  $c_u = 0.25 \pm 0.025$  and  $c_L = 0.2 \pm 0.05$ , [17,19,38,43,44]. Furthermore, the experimental area is located at  $z = (4.6 \pm 0.6)M$  distance from the grid, and  $\epsilon$  is expected to scale as  $z^{-2}$ .

We find that, within experimental error bars, the estimates of  $\epsilon_L$  are in good agreement, with empirical laws for classical turbulence at large scales. In addition, no significant difference is observed between He I and He II.

### B. Estimate of energy transfer at inertial scales

Assuming classical homogeneous isotropic turbulent scalings, the energy transfer rate  $\epsilon_l$  through the inertial scales is classically estimated from the Eulerian second-order structure function [ $S_2^E(r) = \frac{11}{3}C_2(\epsilon_l r)^{\frac{2}{3}}$ ], which in a Lagrangian prospect can robustly be calculated from the particles' relative dispersion statistics [45]. As described below, this method has the benefit to give an estimate of the structure function based on position increments, without requiring the calculation of particles velocities. This way we avoid having to differentiate trajectories individually, which as discussed previously is very sensitive to experimental noise.

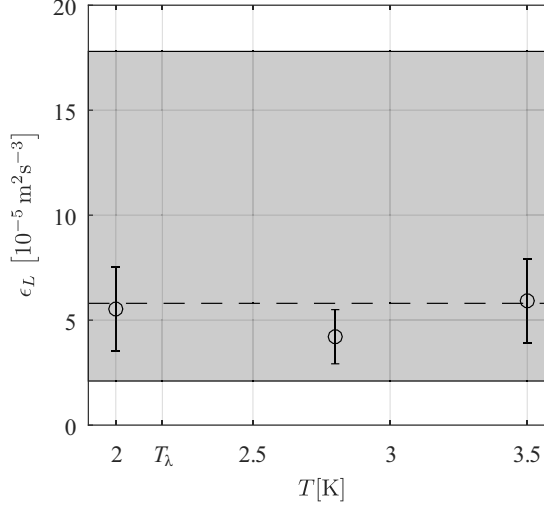


FIG. 11. Dissipation rate  $\epsilon_L$  for the three explored temperatures computed using the  $\sigma_u$  obtained from the ballistic separation method. The gray area shows the range of expected values for  $\epsilon$  according to empirical laws.

### 1. Methodology: Estimate of Eulerian $S_2^E$ from pair separation statistics

The second-order Eulerian structure function can be efficiently estimated from displacement statistics by considering pair statistics. Particle pair dispersion was first introduced in 1926 by Richardson [46] and has become since a classical problem of Lagrangian turbulence. We will only be interested here in the short-time separation regime (also called the ballistic regime [45]), which is the relevant regime to estimate  $S_2^E$ . Consider two particles with an initial separation  $\vec{D}_0$ ; the quadratic relative separation between two particles can be written

$$R_{D_0}^2(t) = \langle |\vec{D}(t) - \vec{D}_0|^2 \rangle,$$

with  $D(t)$  being the instantaneous separation between the particles, and where the average  $\langle \cdot \rangle$  is taken over a set of particles with identical initial separation  $|D_0|$ . By a simple Taylor expansion, one can show that, in the limit  $t \rightarrow 0$  (ballistic regime),  $R_{D_0}^2$  is kinematically related to  $S_2^E$  by

$$R_{D_0}^2(t) = S_2^E(D_0)t^2 + O(t^3). \quad (12)$$

By fitting a quadratic relation for the early-stage pair separation while sweeping the value of initial separation  $D_0$ , it is possible to infer  $S_2^E(r)$  across scales. Compared to a direct estimate from the velocity increments, this method to estimate  $S_2^E$  has the great benefit to avoid computing the position derivative, thus limiting the amplification of experimental noise.

Note that, in practice, we only consider the relative quadratic separation  $R_{D_{0,x}}^2(t)$  in the  $x$  direction, so that the above-mentioned procedure will give access to the one-component structure function  $S_{2,x}^E(r)$ . In isotropic conditions,  $S_{2,x}^E(r)$  is simply one third of the total structure function  $S_2^E(r)$ .

Finally, assuming classical Kolmogorov scalings for  $S_2^E$ , one can then estimate  $\epsilon$  from  $R_{D_{0,x}}^2(t)$  using the relation (valid only in the limit of small time lags)

$$\frac{R_{D_{0,x}}^2(t)}{\frac{11}{9}C_2D_0^{2/3}} = \epsilon_I^{2/3}t^2 + O(t^3). \quad (13)$$

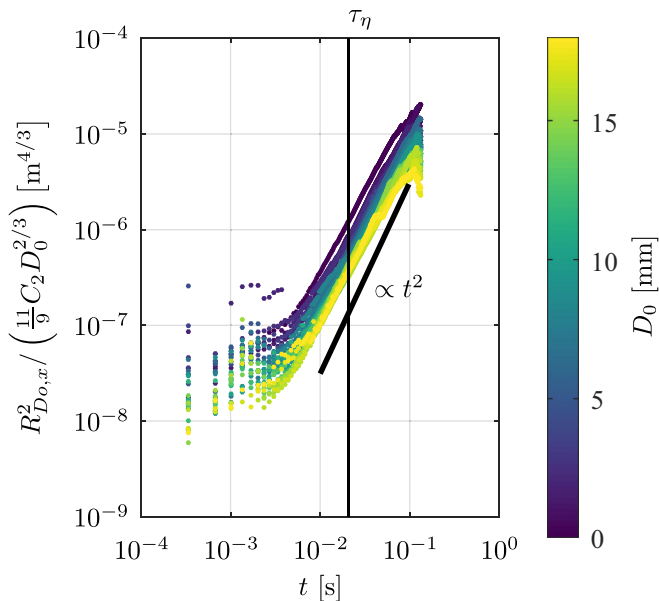


FIG. 12. Time evolution of  $R_{D_0,x}^2 / (\frac{11}{9}C_2 D_0^{2/3})$  in Config. 2 (He I).

## 2. Results

Figure 12 presents the time evolution of the normalized mean square separation (in the  $x$  direction)  $R_{D_0,x}^2 / (\frac{11}{9}C_2 D_0^{2/3})$  against  $t$ . Each curve is for a specific bin of initial separation  $D_0$ . The expected ballistic regime is clearly visible for time lags  $t \approx \tau_\eta$ . A deviation from the ballistic regime can be seen at the shortest time lags. This is a signature of the noise in the position measurement: in the limit of a purely random (Brownian-like noise) the particle separation rate is expected to be purely diffusive [ $R^2(t) \propto t$ ], which is consistent with the less steep slope at short times.

By individually fitting each curve in Fig. 12 against  $t^2$ , we can extract the value of the slope  $S_{2,x}^E / (\frac{11}{9}C_2 D_0^{2/3})$  for each initial separation  $D_0$ . Assuming Kolmogorov scaling, we can then assess  $\epsilon_I$  using the relation  $\epsilon_I = (S_{2,x}^E / \frac{11}{9}C_2)^{3/2} D_0$  [see Eq. (13)]. The result of this fitting procedure is shown in Fig. 13 as a function of the initial separation  $D_0$ .

A first important and interesting finding is that Fig. 13 does not highlight any measurable difference between the He I and He II situations. We see a pseudoplateau in the inertial range (we recall that, in the present situation, the integral scale is estimated to be  $L \simeq 14$  mm), indicating a reasonable Kolmogorov scaling. At small scales, one would expect a trivial dissipative scaling  $S_2(D_0) \propto D_0^2$ , and hence the points in Fig. 13 increasing linearly with  $D_0$ , which is clearly inconsistent with the decrease observed at  $D_0 \lesssim 5$  mm. This is primarily due to the fact that small scales are biased by the finite depth of field ( $\delta_{\text{dof}} \simeq 1.4$  mm) of our measurement volume, since we only have access to 2D measurements. Estimates of separation data are therefore accurate only in the limit  $D_0 > \delta_{\text{dof}}$ . In addition, given the dilute nature of our flow there are not enough statistics at small  $D_0$ . For separations  $D_0$  of the order of and smaller than  $\delta_{\text{dof}}$ , the possible overlap of the 2D projection of particles within the depth of field allows for large relative velocities even in the limit of small apparent separations.

We therefore estimate the dissipation rate  $\epsilon_I$  by averaging  $[(S_{2,x}^E / \frac{11}{9}C_2)^{3/2} D_0]$  over the plateau in the range  $6 \text{ mm} < D_0 < 14 \text{ mm}$ , corresponding to inertial scales not significantly affected by the finite depth of field bias, delimited by the two vertical dashed lines in Fig 13.

The corresponding values of  $\epsilon_I$  as a function of the operating temperature is shown in Fig. 14. It is found that, within error bars, the inertial scale estimate  $\epsilon_I$  is in good agreement both with

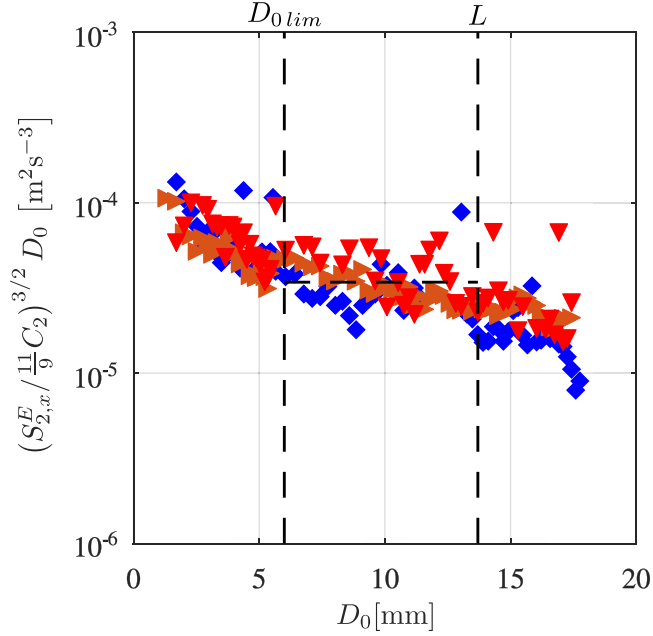


FIG. 13. Slope  $S_{2,x}^E$  of the quadratic relative separation  $R_{D_0}^2$  versus  $t^2$ , normalized and scaled to show the inferred dissipation  $\epsilon_I$  as a function of the initial separation  $D_0$ . The horizontal dashed line shows the average value of  $\epsilon_I$  over relevant length scales (see text for details).  $\blacktriangledown$  He I (#1),  $\blacktriangleright$  He I (#2),  $\blacklozenge$  He II (#3).

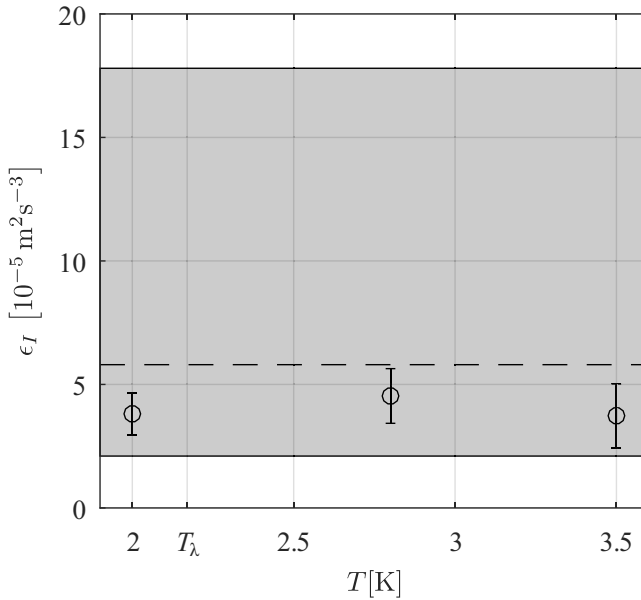


FIG. 14. Dissipation rate  $\epsilon_I$  for the three explored temperatures computed the function estimated from pair separation. The gray area shows the range of expected values for  $\epsilon$  according to empirical laws.

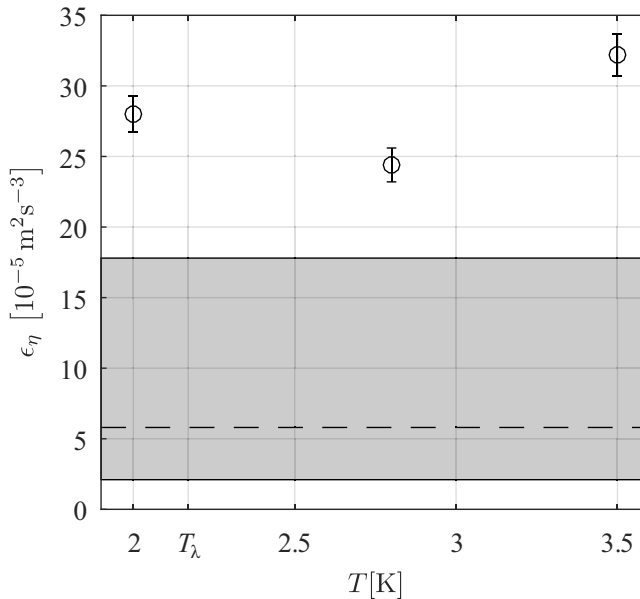


FIG. 15. Dissipation rate  $\epsilon_\eta$  vs temperature  $T$  at dissipative scales.

empirical laws and with the estimate  $\epsilon_L$  discussed in the previous section. In particular, no difference is observed between He II and He I.

### C. Dissipative scales

Estimation of the dissipation at dissipative scales requires the analysis of small-scale information. In the Eulerian context, this usually goes back to the definition of dissipation  $\epsilon_\eta = 2\nu\Omega^2$  (with  $\Omega^2$  being the enstrophy), which in homogeneous isotropic turbulence can simply be rewritten in terms of a single-component (say  $u$ ) spatial derivative :  $\epsilon_\eta = 15\nu\partial_x u$ . This requires measurements with high spatial resolution, allowing us to take well-resolved spatial derivatives of the velocity field. In the context of Lagrangian measurements, as in the present study, the relevant small-scale quantity is the Lagrangian acceleration (rather than the velocity gradient), which is related to the dissipation rate via the Heisenberg-Yaglom relation:

$$\sigma_{ax}^2 = a_0 \epsilon_\eta^{3/2} \nu^{-1/2}. \quad (14)$$

In this relation  $\sigma_{ax}$  is the standard deviation of horizontal acceleration fluctuations and  $a_0$  is a dimensionless coefficient that is empirically known in classical turbulence (from experimental and numerical studies; see, for instance, the review article of Toschi and Bodenschatz [47]) and which is known to depend on the Reynolds number following an empirical law  $a_0 \simeq 0.85R_\lambda^{-25}$ , see Ref. [48].

Unfortunately, considering the noise issues previously discussed regarding the direct estimates of velocity statistics, it is unlikely that our measurements are sufficiently well resolved at small temporal scales to actually resolve Lagrangian derivatives required to estimate acceleration, as taking second-order derivatives is extremely sensitive to experimental noise.

Still we attempted to perform this estimate. The acceleration is calculated by convolution of particles trajectories with a second-derivative Gaussian kernel, as classically done in Lagrangian studies to estimate filtered derivatives [33], with the same filtering parameters (in particular the same filter width as for the direct velocity estimates previously discussed in Sec. V). From these data we calculate the acceleration variance  $\sigma_{ax}$ , which is then used to estimate the small-scale dissipation rate from the Heisenberg-Yaglom relation. The corresponding results are plotted as a function of the operating temperature in Fig. 15.

As one can see in Fig. 15, our experimental data do not match the expected values from the literature, neither in He I nor in He II. Consequently, this result cannot be attributed to a particular behavior of II but rather to an insufficient temporal resolution to accurately estimate the acceleration at dissipative scales. Efforts have been put at present on the experimental side in order to improve this and perform measurements with sufficient resolution at inertial and dissipative scales.

## VII. CONCLUSION

A oscillating grid experiment has been developed in order to study homogeneous and isotropic turbulence in normal and superfluid helium. Lagrangian trajectories were obtained using 2D particle tracking of hollow glass spheres of diameter  $85\ \mu\text{m}$ . Special emphasis was put on the validation of the particle seeding procedure, through the use of Voronoï tessellation, and additionally we have compared thoroughly every observable with standard data obtained at room temperature to conclude that our setup produces the expected canonical flow.

The Lagrangian tracks allowed us to build a complete turbulent energy budget by estimating the energy-injection rate at an integral scale, the rate through inertial scales, and then the energy dissipation rate at dissipative scale. The most important result is that, independent of the actual value of the terms, no difference could be found between He I and He II within experimental uncertainty. The energy injection rate  $\epsilon_L = \sigma_u^3/L$  has been obtained by two methods, which allowed us to discuss the contribution of experimental noise in the estimation of the standard deviation of the velocity. The results compare very well with oscillating grid experiments. The rate  $\epsilon_I$  was obtained by estimating the Eulerian function from particle pair separation. As expected in the framework of HIT,  $\epsilon_I$  were found to match the energy-injection rate  $\epsilon_L$ . Finally, we used the Heisenberg-Yaglom relation to estimate the energy-dissipation rate  $\epsilon_\eta$  at small scale. We found a large discrepancy with the other two terms of the energy budget but, again, we found consistent values in He I and He II, which proved to be overestimated in both cases. The larger value was attributed to some limitations in our 2D measurement setup, with a finite depth of field.

This motivates us to focus future experimental projects towards small scales, with smaller particles or larger dissipative scales, low noise, and 3D measurements while continuing our strategy of direct comparison between helium I and II.

## ACKNOWLEDGMENTS

We would like to thank the anonymous referee who participated greatly to improve the quality of this paper. We would also like to thank Philippe Charvin and Florian Bancel for their support in designing and running the experiment. This research work was funded by the CEA (grant CFR-2012) and the optical setup was funded by the LANEF program (grant ANR-10-LABX-51-01).

- 
- [1] W. F. Vinen and J. J. Niemela, Quantum turbulence, *J. Low Tem. Phys.* **128**, 167 (2002).
  - [2] J. Maurer and P. Tabeling, Local investigation of superfluid turbulence, *Europhys. Lett.* **43**, 29 (1998).
  - [3] J. Salort, C. Baudet, B. Castaing, B. Chabaud, F. Daviaud, T. Didelot, P. Diribarne, B. Dubrulle, Y. Gagne, F. Gauthier *et al.*, Turbulent velocity spectra in superfluid flows, *Phys. Fluids* **22**, 125102 (2010).
  - [4] L. Skrbek, Energy spectra of quantum turbulence in He II and 3He-B: A unified view, *JETP Lett.* **83**, 127 (2006).
  - [5] K. L. Chopra and J. B. Brown, Suspension of particles in liquid helium, *Phys. Rev.* **108**, 157 (1957).
  - [6] T. A. Kitchens, W. A. Steyert, R. D. Taylor, and P. P. Craig, Flow Visualization in He II: Direct Observation of Helmholtz Flow, *Phys. Rev. Lett.* **14**, 942 (1965).
  - [7] M. Murakami and N. Ichikawa, Flow visualization study of thermal counterflow jet in He II, *Cryogenics* **29**, 438 (1989).

- [8] T. Zhang, D. Celik, and S. Van Sciver, Tracer particles for application to PIV studies of liquid helium, *J. Low Temp. Phys.* **134**, 985 (2004).
- [9] G. P. Bewley, M. S. Paoletti, D. P. Lathrop, and K. R. Sreenivasan, Visualization of quantized vortex dynamics, in *IUTAM Symposium on Computational Physics and New Perspectives in Turbulence*, edited by Y. Kaneda (Springer Netherlands, Dordrecht, 2008), Vol. 4, pp. 163–170.
- [10] M. S. Paoletti, R. B. Fiorito, K. R. Sreenivasan, and D. P. Lathrop, Visualization of superfluid helium flow, *J. Phys. Soc. Jpn.* **77**, 111007 (2008).
- [11] M. L. Mantia, T. V. Chagovets, M. Rotter, and L. Skrbek, Testing the performance of a cryogenic visualization system on thermal counterflow by using hydrogen and deuterium solid tracers, *Rev. Sci. Instrum.* **83**, 055109 (2012).
- [12] M. La Mantia, Particle trajectories in thermal counterflow of superfluid helium in a wide channel of square cross section, *Phys. Fluids* **28**, 024102 (2016).
- [13] P. Svancara and M. La Mantia, Flows of liquid 4He due to oscillating grids, *J. Fluid Mech.* **832**, 578 (2017).
- [14] Y. Tang, S. Bao, T. Kanai, and W. Guo, Statistical properties of homogeneous and isotropic turbulence in He II measured via particle tracking velocimetry, *Phys. Rev. Fluids* **5**, 084602 (2020).
- [15] B. Mastracci and W. Guo, Exploration of thermal counterflow in He II using particle tracking velocimetry, *Phys. Rev. Fluids* **3**, 063304 (2018).
- [16] N. F. Sy, M. Bourgoïn, P. Diribarne, M. Gibert, and B. Rousset, Oscillating grid high Reynolds experiments in superfluid, in *Proceedings of the 15th European Turbulence Conference, 2015 (ETC15)* (TU Delft, 2015), No. 318.
- [17] E. J. Hopfinger and J.-A. Toly, Spatially decaying turbulence and its relation to mixing across density interfaces, *J. Fluid Mech.* **78**, 155 (1976).
- [18] H. J. S. Fernando and I. P. D. De Silva, Note on secondary flows in oscillating-grid, mixing-box experiments, *Phys. Fluids A* **5**, 1849 (1993).
- [19] I. P. D. D. Silva and H. J. S. Fernando, Oscillating grids as a source of nearly isotropic turbulence, *Phys. Fluids* **6**, 2455 (1994).
- [20] S. R. Stalp, L. Skrbek, and R. J. Donnelly, Decay of Grid Turbulence in a Finite Channel, *Phys. Rev. Lett.* **82**, 4831 (1999).
- [21] C. M. White, A. N. Karpetsis, and K. R. Sreenivasan, High-Reynolds-number turbulence in small apparatus: grid turbulence in cryogenic liquids, *J. Fluid Mech.* **452**, 189 (2002).
- [22] I. P. D. D. Silva and H. J. S. Fernando, Some aspects of mixing in a stratified turbulent patch, *J. Fluid Mech.* **240**, 601 (1992).
- [23] K. R. Sreenivasan, On the scaling of the turbulence energy dissipation rate, *Phys. Fluids* **27**, 1048 (1984).
- [24] S. Babuin, E. Varga, L. Skrbek, E. Lévêque, and P.-E. Roche, Effective viscosity in quantum turbulence: A steady-state approach, *Europhys. Lett.* **106**, 24006 (2014).
- [25] B. Rousset, D. Chatain, D. Beysens, and B. Jager, Two-phase visualization at cryogenic temperature, *Cryogenics* **41**, 443 (2001).
- [26] S. P. McKenna and W. R. McGillis, Observations of flow repeatability and secondary circulation in an oscillating grid-stirred tank, *Phys. Fluids* **16**, 3499 (2004).
- [27] R. Monchaux, Measuring concentration with Voronoï diagrams: the study of possible biases, *New J. Phys.* **14**, 095013 (2012).
- [28] T. Zhang and S. W. Van Sciver, Large-scale turbulent flow around a cylinder in counterflow superfluid4He (He II), *Nat. Phys.* **1**, 36 (2005).
- [29] W. Guo, M. La Mantia, D. P. Lathrop, and S. W. Van Sciver, Visualization of two-fluid flows of superfluid helium-4, *Proc. Natl. Acad. Sci.* **111**, 4653 (2014).
- [30] R. Monchaux, M. Bourgoïn, and A. Cartellier, Preferential concentration of heavy particles: A Voronoï analysis, *Phys. Fluids* **22**, 103304 (2010).
- [31] J.-S. Ferenc and Z. Neda, On the size distribution of Poisson Voronoï cells, *Phys. A (Amsterdam, Neth.)* **385**, 518 (2007).
- [32] N. T. Ouellette, Particle tracking, [https://web.stanford.edu/~nto/software\\_tracking.shtml](https://web.stanford.edu/~nto/software_tracking.shtml) (2011), accessed 01-June-2020.

- [33] N. Mordant, A. M. Crawford, and E. Bodenschatz, Experimental Lagrangian acceleration probability density function measurement, *Physica D* **193**, 245 (2004).
- [34] N. Mordant, A. M. Crawford, and E. Bodenschatz, Three-Dimensional Structure of the Lagrangian Acceleration in Turbulent Flows, *Phys. Rev. Lett.* **93**, 214501 (2004).
- [35] N. T Ouellette, H. Xu, M. Bourgoïn, and E. Bodenschatz, Small-scale anisotropy in Lagrangian turbulence, *New J. Phys.* **8**, 102 (2006).
- [36] N. T Ouellette, H. Xu, M. Bourgoïn, and E. Bodenschatz, An experimental study of turbulent relative dispersion models, *New J. Phys.* **8**, 109 (2006).
- [37] S. Klein, M. Gibert, A. Bérut, and E. Bodenschatz, Simultaneous 3D measurement of the translation and rotation of finite-size particles and the flow field in a fully developed turbulent water flow, *Meas. Sci. Technol.* **24**, 024006 (2013).
- [38] A. Eidelman, T. Elperin, A. Kapusta, N. Kleeorin, A. Krein, and I. Rogachevskii, Oscillating grids turbulence generator for turbulent transport studies, *Nonlinear Processes Geophys.* **9**, 201 (2002).
- [39] M. J. Drayton, Eulerian and Lagrangian studies of inhomogeneous turbulence generated by an oscillating grid, Ph.D. thesis, University of Cambridge, 1993, <https://ethos.bl.uk/OrderDetails.do?uin=uk.bl.ethos.318099>.
- [40] N. Machicoane, P. Huck, and R. Volk, Estimating two-point statistics from derivatives of a signal containing noise: Application to auto-correlation functions of turbulent Lagrangian tracks, *Rev. Sci. Instrum.* **88**, 065113 (2017).
- [41] W. F. Vinen and D. Shoenberg, Mutual friction in a heat current in liquid helium II III. Theory of the mutual friction, *Proc. R. Soc. London Ser. A* **242**, 493 (1957).
- [42] K. R. Sreenivasan, An update on the energy dissipation rate in isotropic turbulence, *Phys. Fluids* **10**, 528 (1998).
- [43] E. Villermaux, B. Sixou, and Y. Gagne, Intense vortical structures in grid-generated turbulence, *Phys. Fluids* **7**, 2008 (1995).
- [44] S. M. Thompson and J. S. Turner, Mixing across an interface due to turbulence generated by an oscillating grid, *J. Fluid Mech.* **67**, 349 (1975).
- [45] M. Bourgoïn, Turbulent pair dispersion as a ballistic cascade phenomenology, *J. Fluid Mech.* **772**, 678 (2015).
- [46] L. F. Richardson, Atmospheric diffusion shown on a distance-neighbour graph, *Proc. R. Soc. London Ser. A* **110**, 709 (1926).
- [47] F. Toschi and E. Bodenschatz, Lagrangian properties of particles in turbulence, *Annu. Rev. Fluid Mech.* **41**, 375 (2009).
- [48] G. A. Voth, A. La Porta, A. M. Crawford, J. Alexander, and E. Bodenschatz, Measurement of particle accelerations in fully developed turbulence, *J. Fluid Mech.* **469**, 121 (2002).